

# Unveiling the stellar origin of the Wolf-Rayet nebula NGC 6888 through infrared observations

G. Rubio<sup>1,2\*</sup>, J.A. Toalá<sup>3†</sup>, P. Jiménez-Hernández<sup>3</sup>, G. Ramos-Larios<sup>1,2</sup>, M.A. Guerrero<sup>4</sup>,  
V. M. A. Gómez-González<sup>3</sup>, E. Santamaría<sup>1,2</sup> and J.A. Quino-Mendoza<sup>1,2</sup>

<sup>1</sup>CUCEI, Universidad de Guadalajara, Blvd. Marcelino García Barragán 1421, 44430, Guadalajara, Jalisco, Mexico

<sup>2</sup>Instituto de Astronomía y Meteorología, Dpto. de Física, CUCEI, Av. Vallarta 2602, 44130, Guadalajara, Jalisco, Mexico

<sup>3</sup>Instituto de Radioastronomía y Astrofísica (IRyA), UNAM Campus Morelia, Apartado postal 3-72, 58090 Morelia, Michoacán, Mexico

<sup>4</sup>Instituto de Astrofísica de Andalucía, IAA-CSIC, Glorieta de la Astronomía s/n, 18008, Granada, Spain

14 September 2020

## ABSTRACT

We present a comprehensive infrared (IR) study of the iconic Wolf-Rayet (WR) wind-blown bubble NGC 6888 around WR 136. We use *Wide-field Infrared Survey Explorer* (WISE), *Spitzer* IRAC and MIPS and *Herschel* PACS IR images to produce a sharp view of the distribution of dust around WR 136. We complement these IR photometric observations with *Spitzer* IRS spectra in the 5–38  $\mu\text{m}$  wavelength range. The unprecedented high-resolution IR images allowed us to produce a clean spectral energy distribution, free of contamination from material along the line of sight, to model the properties of the dust in NGC 6888. We use the spectral synthesis code Cloudy to produce a model for NGC 6888 that consistently reproduces its optical and IR properties. Our best model requires a double distribution with the inner shell composed only of gas, whilst the outer shell requires a mix of gas and dust. The dust consists of two populations of grain sizes, one with small sized grains  $a_{\text{small}}=[0.002\text{--}0.008]\ \mu\text{m}$  and another one with large sized grains  $a_{\text{big}}=[0.05\text{--}0.5]\ \mu\text{m}$ . The population of big grains is similar to that reported for other red supergiants stars and dominates the total dust mass, which leads us to suggest that the current mass of NGC 6888 is purely due to material ejected from WR 136, with a negligible contribution of swept up interstellar medium. The total mass of this model is  $25.5^{+4.7}_{-2.8}\ M_{\odot}$ , a dust mass of  $M_{\text{dust}}=0.14^{+0.03}_{-0.01}\ M_{\odot}$ , for a dust-to-gas ratio of  $5.6 \times 10^{-3}$ . Accordingly, we suggest that the initial stellar mass of WR 136 was  $\lesssim 50\ M_{\odot}$ , consistent with current single stellar evolution models.

**Key words:** stars: evolution — stars: individual: NGC 6888, WR 136 – stars: winds, outflows — infrared: ISM — stars: Wolf-Rayet

## 1 INTRODUCTION

Wolf-Rayet (WR) stars are formed as the result of the evolution of O-type stars with initial masses  $> 20\ M_{\odot}$  (Ekström et al. 2012). The single stellar evolutionary scenario suggests that, before entering the WR phase, these stars become red supergiant (RSG) or luminous blue variable (LBV) stars whose slow winds ( $v_{\infty} \approx 30\text{--}200\ \text{km s}^{-1}$ ) strip them from their hydrogen-rich outer layers producing dense structures around them (e.g., Cox et al. 2012; Morris et al. 2017). Furthermore, observational evidence suggests that the majority of massive stars are born in binary systems (Sana et al. 2012), which affect their evolution and, consequently, the production of WR stars (Eldridge et al. 2017; Mason et al. 2009). Mass transfer between the binary components or the ejection of a common envelope might also strip the hydrogen-rich envelope of one of the components creating a WR star (see, e.g., Göteborg et al. 2018; Ivanova 2011, and references therein). Nevertheless, WR stars exhibit strong fast winds ( $v_{\infty} \approx 1500\ \text{km s}^{-1}$ ,  $\dot{M} \approx 10^{-5}\ M_{\odot}\ \text{yr}^{-1}$ ; Hamann et al. 2006) that

sweep and compress the previously ejected material. This interaction produces a wind-blown bubble around the WR star and, at the same time, the strong UV flux from the progenitor star ionizes the material (e.g., García-Segura & Mac Low 1995). The combination of all these effects produces WR nebulae (see Chu 1981).

WR nebulae have radii as large as  $\sim 10\ \text{pc}$  (e.g., Toalá et al. 2012, 2017) and in some cases exhibit multiple shells due to the eruptive mass ejection of the progenitor star (Marston 1995a; Marston et al. 1999). This demonstrates the powerful energy injection of very massive stars leveraging their role as one of the main actors shaping and enriching the interstellar medium (ISM). Spectroscopic studies of WR nebulae can unveil the production of heavy elements in their interiors, which can be used to test stellar evolution models and the chemical gradients in their host galaxies (Esteban, et al. 2016; Méndez-Delgado et al. 2020). However, these structures are short-lived and therefore seldomly detected. WR nebulae will experience hydrodynamical instabilities causing them to break and to dissipate into the ISM within a few times  $10^4\ \text{yr}$  (Freyer et al. 2006; Toalá & Arthur 2011). That is, not many WR stars exhibit associated nebulae (Gruendl et al. 2000; Stock & Barlow 2010), thus, producing

\* E-mail: grubio@idec.edu.mx

† E-mail: j.toala@irya.unam.mx

detailed studies of known WR nebulae can bring us closer to understanding the violent impact of massive stars in the ISM.

Massive stars have been appointed to be laboratories for studying dust formation, processing and evolution (Wachter et al. 2010; Gvaramadze et al. 2010; Verhoelst et al. 2009). During the RSG and LBV phases these stars reduce their effective temperature,  $T_{\text{eff}} \leq 10^4$  K, allowing the formation of dust in their surroundings. The details of these processes depend on whether the star evolved through a RSG or LBV phase. RSG stars, with their enhanced mass-loss rates ( $\dot{M} \lesssim 10^{-4} M_{\odot} \text{ yr}^{-1}$ ), may form dust-rich shells with dust sizes as large as a few times  $0.1 \mu\text{m}$  (see Scicluna et al. 2015, and references therein). Meanwhile, the eruptive nature of the high mass-loss rate of LBV stars ( $\dot{M} \gtrsim 10^{-3} M_{\odot} \text{ yr}^{-1}$ ; Weis 2001) may cause the dust to be shielded from stellar radiation, allowing it to grow to sizes as large as  $1 \mu\text{m}$  (Kochanek 2011) as reported for the iconic LBV star  $\eta$  Car (Morris et al. 2017). Dust production can also occur at the interacting wind surface of massive binaries. In particular, carbon-rich WR stars (WC) with OB companions have been found to exhibit dust-rich pinwheel nebulae (e.g., Tuthill et al. 1999; Marchenko et al. 2002). Furthermore, it has been suggested that dust can also form in the ejecta of a common envelope phase around a binary system (Lü et al. 2013).

Dust has been found spatially associated with the brightest optical regions of WR nebulae. Early infrared (IR) studies of WR nebulae showed that dust is thermally-heated by the strong ionizing flux from their progenitor stars (van Buren & McCray 1988). Larger cavities harbouring WR nebulae have also been detected through IR and radio observations and these very likely correspond to the previous bubble carved by the feedback of the progenitor star during the main sequence phase (Marston 1995b, 1996; Arnal & Cappa 1996; Cappa et al. 1996). Marston (1991) presented the analysis of far-IR *IRAS* observations of the WR nebulae NGC 2359, RCW 58 and NGC 6888 and suggested that their dust masses were in the range of  $0.25\text{--}1.3 M_{\odot}$ . Taking into account the typically-adopted dust-to-gas ratio of 0.01, the total nebular masses of these WR nebulae were too large to have a stellar origin. Accordingly, Marston (1991) attributed them to swept up material from the ISM. A subsequent study presented by Mathis, Casinelli & van der Hucht (1992) demonstrated that these mass estimates can change dramatically if the effects of the radiation field from the star are accounted for.

The advent of a new generation of IR satellites provided us with the opportunity of spatially resolve structures in WR nebulae, improving our understanding of dust processing in nebulae around massive stars (see Cichowolski et al. 2020). Furthermore, *Spitzer* and *WISE* have been used to unveil a new population of obscured nebulae around LBV and WR stars (Gvaramadze et al. 2010; Toalá et al. 2015). More recently, *Herschel* observations of M 1-67 around WR 124 were presented by Vamvatira-Nakou et al. (2016). Their radiative transfer model predicted a total nebular mass of  $22 M_{\odot}$  with a dust mass of  $0.26 M_{\odot}$ . These authors predicted dust particles with sizes between 2 and  $10 \mu\text{m}$  in M 1-67, but such large dust particles have never been reported in circumstellar nebulae.

We have started a series of works to analyze publicly available IR observations of WR nebulae using the photoionization code CLOUDY (Ferland et al. 2017) in conjunction with detailed synthetic WR spectra obtained from the state-of-the-art Potsdam Wolf-Rayet Models (PoWR) models (Hamann & Gräfener 2004)<sup>1</sup>. Our most recent work on the WR nebula M 1-67 showed that there is no need for dust with sizes larger than  $1 \mu\text{m}$  to reproduce the nebular and dust properties

(Jiménez-Hernández, Arthur & Toalá 2020, hereinafter Paper I). By combining modern tools we were able to conclude that the origin of M 1-67 might have been due to a common envelope scenario, which makes this WR nebula the first evidence of such process in massive stars.

In this paper we present our analysis of the WR nebula NGC 6888 (a.k.a. the Crescent Nebula; see Fig. 1 top left) around WR 136 (a.k.a. HD 192163), one of the most studied galactic WR nebulae.  $H\alpha$  narrow-band emission images show a filamentary and clumpy structure (Stock & Barlow 2010), which very likely formed as a result of hydrodynamical instabilities generated through the wind-wind interacting scenario (e.g., García-Segura et al. 1996; Toalá & Arthur 2011). An outer *skin* of [O III] emission encompassing the clumpy structure results from the shock of the expanding RSG material pushed by the WR wind (Gruendl et al. 2000; Moore, Hester & Scowen 2000). This [O III] shell also confines the adiabatically-shocked, X-ray-emitting hot bubble (see Toalá et al. 2016, 2014; Wrigge et al. 2005, and references therein).

Several studies have addressed the physical properties of NGC 6888 and in general all these studies result in similar abundances (see Esteban, et al. 2016; Fernández-Martín et al. 2012; Reyes-Pérez et al. 2015; Stock & Barlow 2014, and references therein). Fernández-Martín et al. (2012) suggested that NGC 6888 is mainly composed of three structures: i) an ellipsoidal inner broken structure formed by shocked shells from the WR and RSG stages, ii) an outer spherical shell presumably formed by the breaking of the main sequence (MS) bubble, and iii) a faint structure around the nebula created by the interaction of the MS winds and the local ISM. Using the ionization code CLOUDY, Reyes-Pérez et al. (2015) concluded that NGC 6888 is chemically homogeneous and uniformly filled with low density material,  $1 \text{ cm}^{-3}$ , in stark contrast to the obvious different morphological components and previous density estimates.

Here we present a complete analysis of the IR emission of NGC 6888. We use images and spectra from *WISE*, *Spitzer* and *Herschel* that cover the  $3\text{--}160 \mu\text{m}$  wavelength range. The images are used to study the distribution of dust in NGC 6888 in comparison with optical images. The spectral energy distribution (SED) in the IR, in combination with publicly available estimates of the abundances and nebular properties, has been used to model the properties of the dust and ionized components of NGC 6888 with the ionization code CLOUDY. Our paper is organised as follows. The observations are presented in Section 2. The analyses of the images, the IR photometry, and the IR spectra are presented in Sections 3, 4 and 5, respectively. Our models of NGC 6888 are presented in Section 6. Finally, the discussion and conclusions are presented in Sections 7 and 8.

## 2 OBSERVATIONS

### 2.1 IR images and spectra

All the IR observations used in the present work have been obtained from the NASA/IPAC Infrared Science Archive<sup>2</sup>. Details of the observations such as the telescope, instrument, spectral band, observation date and principal investigator (PI) are listed in Table 1. Archival IR images of NGC 6888 were obtained from *WISE*, *Spitzer* IRAC &

<sup>1</sup> <http://www.astro.physik.uni-potsdam.de/PoWR>

<sup>2</sup> <https://irsa.ipac.caltech.edu/frontpage/>



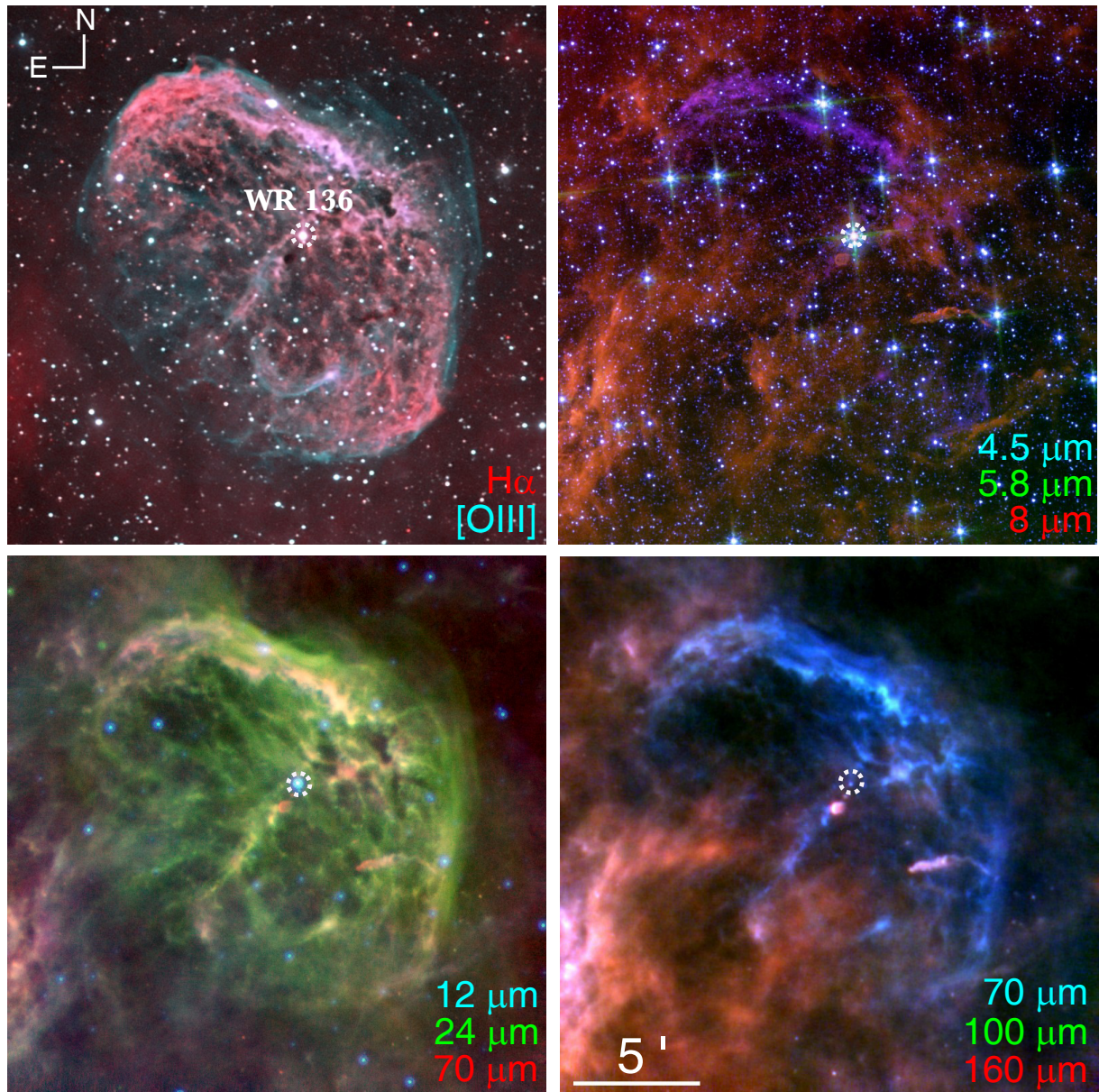


**Figure 1.** Optical and IR views of the WR nebula NGC 6888 showing different morphological structures and the spatial distribution of dust. *Top left:* Colour-composite optical image. *Top right:* Composition of *Spitzer* IRAC images. *Bottom left:* Composition of different mid-IR instruments (*WISE*, *Spitzer* MIPS and *Herschel* PACS). *Bottom right:* Composition of *Herschel* PACS images. The position of WR 136 is shown with a dashed-line circle. All panels have the same field of view.

**Table 1.** Infrared observations of NGC 6888 used in this work.

Telescope	Instrument	Band ( $\mu\text{m}$ )	Obs. date (yyyy-mm-dd)	Obs. ID.	Processing level	PI
<i>Spitzer</i>	IRAC	3.6, 4.5, 5.8, 8.0	2005-10-21	20726	Level 2	J. Hester
	MIPS	24	2005-09-23	20726	Level 2	J. Hester
	IRS	SL (5–15), LL (14–39)	2006-11-09	30544	Level 2	P. Morris
<i>Herschel</i>	PACS	70, 160	2010-12-16	1342212042	Level 3	M. Groenewegen
		100, 160	2010-12-16	1342212040	Level 3	M. Groenewegen
<i>WISE</i>		12	2010-05-14	3031p378_ac51	Level 3	



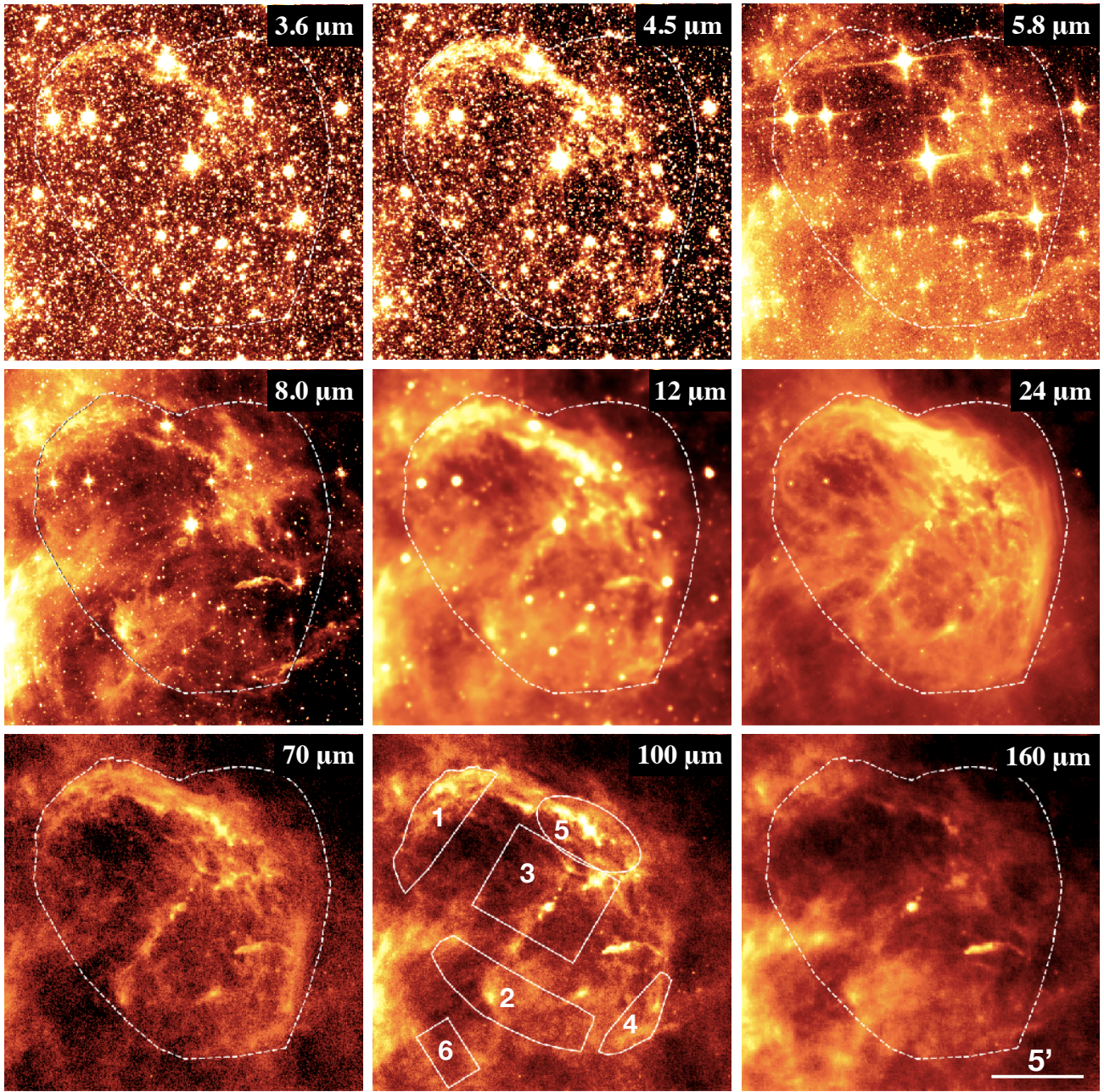


**Figure 2.** IR views of the WR nebula NGC 6888. Each panel correspond to different IR filters (see Table 1). The dashed-line region delimits the optical [O III] emission detected in the optical (see Fig. 1). Regions labelled from 1 to 6 were used to derive the photometric measurements presented in Figure 4. All panels have the same FoV as those in Figure 1. North is up, east to the left.

MIPS, and *Herschel* PACS observations<sup>3</sup>. All available IR images are presented in Figure 2.

The available *Spitzer* Infrared Spectrograph (IRS) observations of NGC 6888 were obtained in *stare* mode (Houck, et al. 2004).

These spectra were obtained with the low- and high-resolution modules, but unfortunately the high-resolution observations do not have suitable regions for background-subtraction. Thus, we inspected these spectra, but no science was obtained from them. The

low-resolution spectra correspond to the Short-Low (SL) and Long-Low (LL) modules covering the 5–38  $\mu\text{m}$  wavelength range. The positions of the low-resolution slits are shown in Figure 3.

The *Spitzer* IRS observations were analysed with the CUBE Builder for IRS Spectra Maps (CUBISM; Smith et al. 2007a) software. CUBISM tasks are used to combine spectra from the same position and to produce one-dimensional spectra. We followed the standard reduction processes, which include background subtraction, characterization of noise in the data and bad pixel removal.

<sup>3</sup> The *Herschel* PACS observations were obtained in the framework of the Mass-loss of Evolved StarS (MESS) project (Groenewegen et al. 2011).



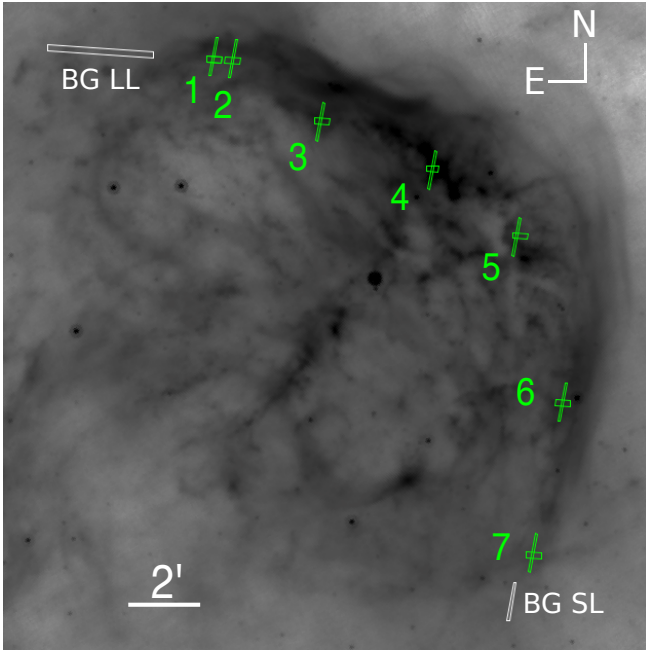


**Figure 3.** *Spitzer* MIPS  $24\ \mu\text{m}$  image of NGC 6888 showing the position of the SL and LL slits (green). The one oriented north to south correspond to SL, the one oriented east to west is LL. The regions used to extract the background are shown with white rectangles.

## 2.2 Optical imaging (OARP)

Optical narrow-band images of NGC 6888 were obtained at the Observatorio Astronómico Robótico Primavera (OARP) operated by the University of Guadalajara (Jalisco, Mexico). The facility is used by undergraduate, graduate, and doctoral programs in physics, astronomy and astrophysics. Recently established, was strategically located just over 20 miles west of Guadalajara, where it was free from light pollution and clearer night sky. The observatory utilizes a 0.32m f/8 CDK (Corrected Dall-Kirkham) telescope equipped with a SBIG STL-6303E/LE commercial camera, which uses a Kodak Enhanced KAF-6303E imaging sensor. This sensor consists of a  $3072 \times 2048$  pixels array with a size of  $9 \times 9$  microns each. In combination with the telescope, it provides a field of view (FoV) of  $37' \times 25'$  and a plate scale of  $0''.73\ \text{pixel}^{-1}$ .

Images of NGC 6888 were obtained on 2019 March 9 and 30 for total exposure times of 2 h in the  $[\text{O III}]$  filter and 1.5 h in the  $\text{H}\alpha$  filter. These filters have central wavelengths and bandwidths of  $\lambda_c = 6563\ \text{\AA}$  and  $\Delta\lambda=30\ \text{\AA}$ , and  $\lambda_c = 5007\ \text{\AA}$  and  $\Delta\lambda=30\ \text{\AA}$ , respectively. The detector was set with a  $2 \times 2$  binning. The data were bias-subtracted and flat-field corrected following standard Image Reduction and Analysis Facility (IRAF) routines (Tody 1993). A colour-composite optical image of NGC 6888 is presented in the top-left panel of Figure 1.

## 3 DUST DISTRIBUTION

Figure 2 presents the different IR images of NGC 6888 in the 3– $160\ \mu\text{m}$  wavelength range. All *Spitzer* IRAC images exhibit a large number of point sources in the vicinity of NGC 6888. The IRAC 3.6 and  $4.5\ \mu\text{m}$  images show a marginal detection coincident with the brightest optical regions of NGC 6888. Some emission is detected

from the NE cap and in a lesser extent from the SW cap. No significant emission from the inner region is detected. The other two IRAC images,  $5.8\ \mu\text{m}$  and  $8.0\ \mu\text{m}$ , trace mostly clumps and filaments of the cold surrounding ISM.

The *Spitzer* MIPS image at  $24\ \mu\text{m}$  traces the continuum emission from dust present in the WR nebula (Toalá et al. 2015).

The *Herschel* PACS  $70\ \mu\text{m}$  image is very similar to that of the *Spitzer* MIPS, but the PACS  $160\ \mu\text{m}$  image rather traces the emission from the cold ISM. Meanwhile, the emission in the *WISE*  $12\ \mu\text{m}$  and *Herschel* PACS  $100\ \mu\text{m}$  images map the contribution from both the nebula and the ISM.

In general, most images presented in Figure 2 trace the morphological features exhibited by the optical image of NGC 6888: the NE and SW caps and the NW blowout. The dark clump and filament described by Fernández-Martín et al. (2012) are clearly visible in the IRAC  $5.8\ \mu\text{m}$  and  $8.0\ \mu\text{m}$  images and in the *Herschel* images, they form part of the cold ISM. For a direct comparison with the optical image, we created three colour-composite IR pictures of NGC 6888 using i) the  $4.5$ ,  $5.8$  and  $8\ \mu\text{m}$  *Spitzer* IRAC images, ii) the  $12$ ,  $24$  and  $70\ \mu\text{m}$  mid-IR images, and iii) the  $70$ ,  $100$  and  $160\ \mu\text{m}$  *Herschel* PACS images. These three images are also presented in Figure 1 along with the optical image of NGC 6888. These combinations of images exhibit in great detail the nebular and dust distribution of NGC 6888. The images confirm the suggestion of Toalá et al. (2014) that NGC 6888 is expanding towards a low-density region along the NW direction, which might be producing the expansion of the blowout. At the same time, the colour-composite IR pictures in Figure 1 indicate that NGC 6888 is placed behind a molecular filament.

The colour-composite IR panels of Figure 1 disclose an interesting feature. In the three IR panels, there is a dark region separating the contribution from NGC 6888 with that of the ISM. This effect is more clearly seen around the NE cap. The lack of IR emission is spatially coincident with the  $[\text{O III}]$  optical emission, which according with Gruendl et al. (2000) traces the expanding shock generated by the wind-wind interaction that created the WR nebula. The diminished IR emission in this layer suggests that dust is being destroyed by the expansion of the shock into the ISM. To further illustrate this, we present in Appendix A close up images of the NE cap of NGC 6888.

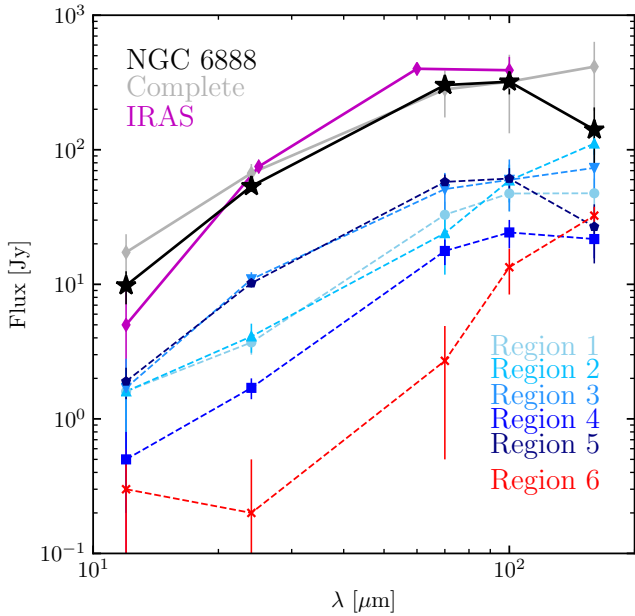
## 4 IR PHOTOMETRY

In order to produce a consistent model of the nebular and dust properties of NGC 6888, we extracted the IR photometry of each available image presented in Figure 2 for  $\lambda \geq 12\ \mu\text{m}$ . We did not use the *Spitzer* IRAC observations because they include the contribution from several nebular lines as well as possible low-ionization emission lines from the ISM. Moreover, the large number of background stars hampers an appropriate selection of the extraction region.

The photometry extraction procedure is described in Paper I. We define extraction regions where the integrated flux can be easily computed by adding all the pixels in the image. The contribution from background stars is excised and thus it is not taken into account for the flux estimate. A similar procedure would be performed for background regions, but it shall be noted that the ISM around NGC 6888 is not homogeneous as revealed by the IR images of NGC 6888 shown in the previous section. To minimise the impact of the spatially-varying background, several background regions surrounding NGC 6888 were selected to compute the same number of background-subtracted fluxes. We emphasize that regions SE from

**Table 2.** IR fluxes of NGC 6888 extracted from different regions.

Instrument	$\lambda_c$ ( $\mu\text{m}$ )	Complete (Jy)	Region 1 (Jy)	Region 2 (Jy)	Region 3 (Jy)	Region 4 (Jy)	Region 5 (Jy)	Region 6 (Jy)	NGC 6888 (Jy)
<i>WISE</i>	12	$17.3 \pm 6.3$	$1.6 \pm 0.6$	$1.6 \pm 0.8$	$1.7 \pm 1.1$	$0.5 \pm 0.3$	$1.9 \pm 0.5$	$0.3 \pm 0.2$	$9.8 \pm 2.7$
<i>Spitzer MIPS</i>	24	$66.9 \pm 11.4$	$3.7 \pm 0.7$	$4.1 \pm 1.0$	$10.9 \pm 1.4$	$1.7 \pm 0.3$	$10.2 \pm 0.7$	$0.2 \pm 0.3$	$53.6 \pm 3.5$
<i>Herschel PACS</i>	70	$281.1 \pm 107.2$	$32.9 \pm 8.2$	$24.0 \pm 12.2$	$51.0 \pm 16.3$	$17.7 \pm 3.8$	$57.7 \pm 7.8$	$2.7 \pm 3.4$	$302.5 \pm 41.0$
<i>Herschel PACS</i>	100	$320.5 \pm 187.9$	$47.3 \pm 12.6$	$59.1 \pm 18.5$	$59.8 \pm 24.9$	$24.3 \pm 5.8$	$61.1 \pm 11.9$	$13.4 \pm 5.0$	$320.5 \pm 62.7$
<i>Herschel PACS</i>	160	$414.4 \pm 220.0$	$47.5 \pm 13.2$	$111.2 \pm 19.4$	$73.3 \pm 26.1$	$21.7 \pm 6.1$	$26.8 \pm 12.5$	$32.4 \pm 5.3$	$140.8 \pm 65.6$

**Figure 4.** SED of the WR nebula NGC 6888 (stars) modeled in the present paper. Different symbols (colours) show the SED of different regions in NGC 6888 as defined in the bottom-central panel of Figure 2. The SED labelled as Complete has been obtained taking into account the whole optical extension of the nebula. The purple SED labelled as IRAS is the photometry used by *Mathis, Casinelli & van der Hucht (1992)*.

NGC 6888 were discarded because they show the strongest contribution from the ISM according to Figures 1 and 2.

The resultant mean and standard deviation of the flux values are used as the flux and its uncertainty ( $\sigma_{\text{back}}$ ), respectively. Nevertheless, a total error must be computed by adding other uncertainties such as that obtained from the calibration ( $\sigma_{\text{cal}}$ ) which depends on each instrument. Thus, the total error can be calculated as

$$\sigma_{\text{tot}} = \sqrt{\sigma_{\text{back}}^2 + \sigma_{\text{cal}}^2} \quad (1)$$

We first extracted the corresponding photometry from an aperture encompassing the emission from the [O III] line which defines the complete nebular extension of NGC 6888 (see Fig. 1). This aperture is shown as a white dashed-line region in most panels of Figure 2. The resultant flux and error values of this region are listed in Table 2 and illustrated in Figure 4 as a SED labelled as Complete. Figure 4 suggests that the Complete photometry of NGC 6888 peaks at wavelengths longer than  $160 \mu\text{m}$ . However, as shown in Figure 2 the

dashed-line region includes a significant contribution (depending on the IR image) from gas that very likely has a ISM origin.

To assess the contribution from the ISM in the SED, we explored the variation of the IR SED from different regions within NGC 6888. The bottom-central panel of Figure 2 shows the different extraction regions here considered. Their corresponding photometry is listed in Table 2 and plotted and compared to the Complete SED in Figure 4. This figure shows that the IR SED extracted from Regions 1–5 exhibit significant differences, but these can be explained by considering the SED of Region 6. The SED of this region, defined from an external filament to NGC 6888, increases with wavelength, suggesting the presence of colder dust in the ISM (see Section 6). Since the emission from NGC 6888 is projected against that of the ISM, this effect should also be present in other regions with different relative contributions. For example, the SED of Region 2, defined at the SE edge of NGC 6888, peaks at long wavelengths, i.e., it shows noticeable contribution from the ISM as shown by Region 6.

An inspection of the SED from these different regions led us to conclude that Region 5 has a SED (mostly) free from the contribution from the ISM. Its SED has a peak located around  $\sim 70\text{--}100 \mu\text{m}$  consistent with the IR emission found in other WR nebulae. Assuming that the SED of Region 5 is thus representative of the shape of the SED of NGC 6888, its flux level has been normalised to that of the emission from the whole nebula to create a SED labelled as NGC 6888 that would describe our target. The resultant SED, which we will use to model the dust properties of NGC 6888, is presented in Figure 4 and the corresponding flux values are listed in the last column of Table 2. For comparison we also show in Figure 4 the *IRAS* SED used in *Mathis, Casinelli & van der Hucht (1992)*. The latter has larger fluxes at mostly all wavelengths except at  $12 \mu\text{m}$ . The excess of the *IRAS* photometry compared to that estimated in this work is very likely due to the contribution from material in the line of sight and the point-like sources unresolved in the *IRAS* observations.

## 5 IR SPECTRA

*Spitzer* IRS spectra of NGC 6888 were extracted from the brightest regions following the N-NW-SW direction. The location of the extraction regions, as shown in Figure 3, are labelled as Slit 1 to 7 and correspond to regions with the lowest or negligible contribution from the ISM. The spectra are very similar with a continuum from dust emission. The dominant emission lines in these spectra are those of [Ne II]  $12.8 \mu\text{m}$ , [Ne III]  $15.5 \mu\text{m}$ , [S III]  $18.7$  and  $33.5 \mu\text{m}$ , [S IV]  $10.5 \mu\text{m}$ , [Ar III]  $8.98 \mu\text{m}$ , and [Si II]  $34.8 \mu\text{m}$  (see Fig. 5). Other less intense lines correspond to He I at  $22.9 \mu\text{m}$  and very likely an absorption due to N V at  $29.5 \mu\text{m}$ . The latter implies the presence of gas with temperature around  $\sim 10^5$  K at the mixing layer between the nebular cold ( $\sim 10^4$  K) and the hot X-ray-emitting gas ( $\sim 10^6$  K)



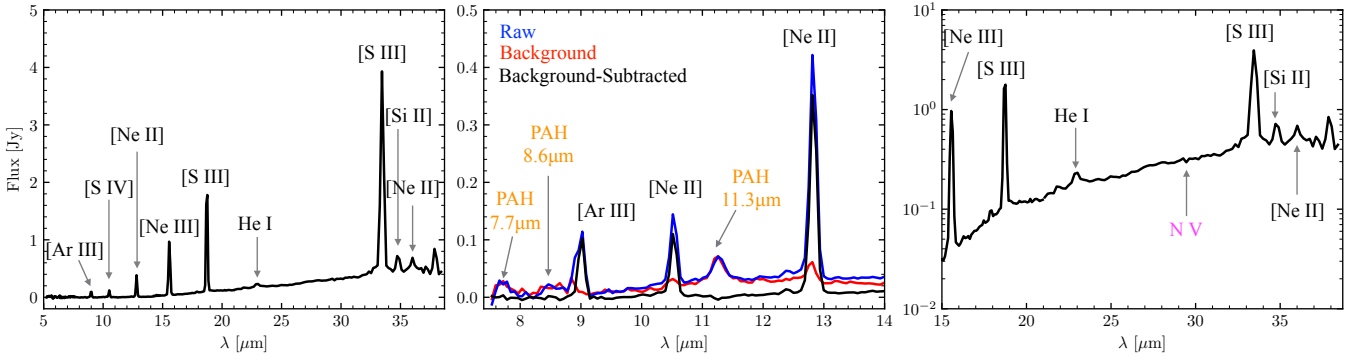


**Figure 5.** Background-subtracted low-resolution IRS spectra (black lines) extracted from Slit 4 as shown in Figure 3. The most prominent lines are labelled. The left panel shows the complete range of the low-resolution spectra while the other two shown different regions of the spectra. The middle panel also shows the background and background-unsubtracted (raw) spectra.

**Table 3.** Fluxes of the emission lines detected in the *Spitzer* IRS observations of NGC 6888. Labels from 1 to 7 represent the extraction regions defined in Figure 3.

Line	$\lambda$ ( $\mu\text{m}$ )	1	2	3	Flux (mJy)	4	5	6	7	Model (mJy)
[Ar III]	8.98	$1.1 \pm 0.2$	$2.3 \pm 0.8$	$6.7 \pm 4.8$	$8.0 \pm 2.1$	$3.9 \pm 3.3$	$0.5 \pm 1.9$	$0.3 \pm 1.1$	1.9	
[S IV]	10.5	$0.2 \pm 0.05$	$0.7 \pm 0.3$	$5.6 \pm 3.9$	$8.4 \pm 2.2$	$3.1 \pm 2.7$	$0.4 \pm 1.6$	$0.1 \pm 0.5$	2.2	
[Ne II]	12.8	$5.2 \pm 0.1$	$4.3 \pm 0.5$	$5.4 \pm 1.4$	$6.1 \pm 0.7$	$3.3 \pm 1.4$	$0.9 \pm 0.9$	$1.3 \pm 1.0$	1.4	
[Ne III]	15.5	$2.9 \pm 0.004$	$3.1 \pm 0.04$	$6.4 \pm 0.05$	$10.8 \pm 0.03$	$3.0 \pm 0.005$	$1.2 \pm 0.03$	$1.0 \pm 0.05$	2.5	
[S III]	18.7	$8.6 \pm 0.01$	$9.3 \pm 0.2$	$12.4 \pm 0.2$	$17.4 \pm 0.08$	$5.7 \pm 0.01$	$2.1 \pm 0.09$	$2.8 \pm 0.3$	9.3	
[S III]	33.5	$19.1 \pm 0.02$	$20.2 \pm 0.04$	$26.1 \pm 0.04$	$34.9 \pm 0.05$	$13.0 \pm 0.03$	$5.8 \pm 0.03$	$6.7 \pm 0.05$	22.6	
[Si II]	34.8	$2.9 \pm 0.02$	$2.4 \pm 0.02$	$2.8 \pm 0.02$	$2.9 \pm 0.03$	$1.8 \pm 0.02$	$1.4 \pm 0.02$	$1.8 \pm 0.02$	7.8	
$n_e$ ([S III])	[ $\text{cm}^{-3}$ ]	420	440	470	520	400	230	350	340	

filling NGC 6888 (e.g., Gruendl et al. 2004; Fang et al. 2016). As an example, we show in Figure 5 the spectrum from Slit 4 with the most prominent lines labelled.

The IRS spectra can be used to look for the presence of molecules in NGC 6888 such as  $\text{H}_2$  and polycyclic aromatic hydrocarbons (PAHs) similarly to other nebulae around evolved stars such as planetary nebulae (see, e.g., Mata et al. 2016; Fang et al. 2018; Toalá et al. 2019, and references therein) and, according to St-Louis et al. (1998), the interstellar nebula around WR 7 (NGC 2359). PAH features appear in the spectra of NGC 6888, but, after subtracting the background spectra, these disappear as illustrated in the middle panel of Figure 5 showing the spectral range including the 7.7, 8.6 and 11.3  $\mu\text{m}$  PAH features. Furthermore, no  $\text{H}_2$  lines are detected in the IRS spectra of NGC 6888.

We used the PAHFIT routines (Smith et al. 2007b) to measure the line intensities and errors for each line for all 7 spectra. The ions, flux and errors of the most prominent lines are listed in Table 3. This table shows clear variations in the measured lines from slit to slit. In particular, emission lines from the spectrum 4 exhibit the largest fluxes. We attribute these differences to the variations of the physical properties within the slit positions, e.g., due to the clumpy distribution of gas in NGC 6888. To corroborate this, we have computed the electron densities ( $n_e$ ) using the [S III] 18.7 and 33.5  $\mu\text{m}$  with PYNEB (Luridiana et al. 2015). The  $n_e$  ([S III]) values are listed in the bottom row of Table 3 for each slit position and, indeed, show that Slit 4 has the largest density estimate.

## 6 DUST MODELING

As a first approximation to the dust temperature ( $T_{\text{dust}}$ ) and mass ( $M_{\text{dust}}$ ), we fitted a modified blackbody (MBB) model to the IR SED of NGC 6888 with  $\lambda \geq 70 \mu\text{m}$ . Under the assumption that dust is optically thin and that all the dust has a single temperature, the MBB can be expressed as

$$F_\nu = \kappa_{\nu_0} \left( \frac{\nu}{\nu_0} \right)^\beta M_{\text{dust}} \frac{B_\nu(T_{\text{dust}})}{d^2}, \quad (2)$$

where  $B_\nu(T_{\text{dust}})$  is the Planck function and  $\kappa_{\nu_0}$  is the dust emissivity adopted to be  $\kappa_{\nu_0} = 27.1 \text{ g cm}^{-2}$  at the reference wavelength  $\lambda = 100 \mu\text{m}$  (Draine 2003). We fitted the *Herschel* photometry taking  $\beta$ ,  $T_{\text{dust}}$  and  $M_{\text{dust}}$  as free parameters. The best fit that minimises  $\chi^2$  corresponds to  $\beta = 2.7 \pm 0.6$ ,  $T_{\text{dust}} = 29.3 \pm 0.3 \text{ K}$  and  $M_{\text{dust}} = 0.69 \pm 0.04 M_\odot$ . Similar temperatures for WR nebulae have been previously estimated with *IRAS* observations (e.g., Marston 1991). However, there is a known degeneracy between  $\beta$  and  $T_{\text{dust}}$  (Juvella et al. 2013) and thus, we computed another model by fixing  $\beta = 2$  that resulted in  $T_{\text{dust}} = 34.4 \pm 0.8 \text{ K}$  and  $M_{\text{dust}} = 0.32 \pm 0.04 M_\odot$ . We note that the MBB fits are not meant to reproduce the complete IR photometry of NGC 6888, but they can be useful to estimate the temperature of the large grain population, another constrain to our detailed model (see below). Nevertheless, these approximations reveal that the dust grains must be present in a wide range of sizes and temperatures. These two MBB models are plotted in Figure 6 in

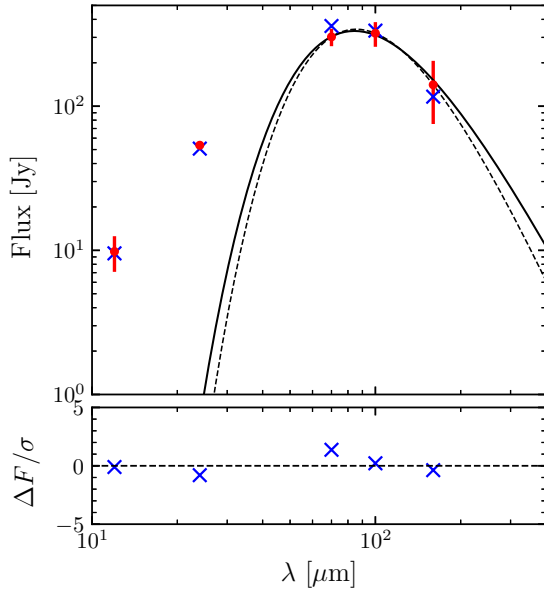


**Figure 6.** Observed IR SED of NGC 6888 (red dots) compared to the synthetic IR SED of our best fit model (blue crosses). The solid and dashed lines correspond to a MBB model with fixed  $\beta = 2$  ( $T_{\text{dust}}=34.4\pm 0.8$  K) and a MBB model with  $\beta$  as a free parameter ( $\beta=2.7\pm 0.6$ ,  $T_{\text{dust}}=29.3\pm 0.3$  K), respectively. The bottom panel shows the residuals between the observed and synthetic IR SED.

comparison with the observed IR SED. To further illustrate the differences with the physical properties of the material in the surrounding ISM, we also estimated the dust temperature for the photometry extracted for Region 6 (see Figures 2 and 4) probing this is ISM. The dust temperature for this emission is lower,  $T_{\text{ISM}}=16.7\pm 0.4$  K, as expected for cold ISM dust (see [Ostrovskii et al. 2020](#), and references therein).

Our goal is to produce a characterization of the dust properties in NGC 6888 consistent with the nebular optical properties. For this, we used the spectral synthesis and plasma simulation code CLOUDY (version 17.01; [Ferland et al. 2017](#)) coupled with the PYCLOUDY libraries ([Morisset 2013](#)). The input parameters required by CLOUDY are i) the form of the incident spectrum (a model of the spectrum of WR 136), ii) the density distribution, iii) abundances, and iv) the dust properties (chemical composition and size distribution).

With these, CLOUDY is able to produce an emission model which is subsequently processed with the help of PYCLOUDY to create synthetic optical long-slit observations. Furthermore, synthetic IR SED photometry is produced by using the transmission curves from the different IR instruments used here<sup>4</sup>. The synthetic observations are then compared to previously published optical studies of NGC 6888 and the IR observations (spectra and IR SED) presented in the previous sections to assess the validity of our models.

We started our modeling adopting the most recent abundances determinations reported by [Esteban, et al. \(2016\)](#), which correspond to 10 m Gran Telescopio de Canarias (GTC) OSIRIS spectroscopic

<sup>4</sup> The transmission curves of the *WISE*, *Spitzer* and *Herschel* instruments were obtained from <http://svo2.cab.inta-csic.es/theory/fps/index.php?mode=browse>

**Table 4.** Elemental abundances of NGC 6888 in units of  $12+\log(X/H)$  reported for the slit A6 in [Esteban, et al. \(2016\)](#) (E2016), [Mesa-Delgado \(2014\)](#) (MD2014) and those used by [Reyes-Pérez et al. \(2015\)](#) (RP2015). The last column shows the abundances adopted for our model.

Element	E2016	MD2014	RP2015	Model
He	$11.23\pm 0.06$	$11.21\pm 0.03$	11.21	11.23
O	$8.19\pm 0.13$	$8.20\pm 0.09$	8.20	8.05
C	–	$8.86\pm 0.31$	8.86	8.86
N	$8.27\pm 0.18$	$8.54\pm 0.20$	8.40	8.68
Ne	$7.51\pm 0.78$	$7.51\pm 0.20$	7.51	7.78
S	$6.92\pm 0.21$	$6.77\pm 0.20$	7.10	6.92
Cl	$4.99\pm 0.15$	–	–	4.84
Ar	$6.41\pm 0.11$	$6.41\pm 0.11$	6.41	6.41

**Table 5.** Emission lines for region A6 of NGC 6888 in [Esteban, et al. \(2016\)](#) compared to the predictions from our model. All line fluxes are normalized with respect to  $H\beta=100$ .

Line	$\lambda$ (Å)	<a href="#">Esteban, et al. (2016)</a> (Slit A6)	Model
[O II]	3726	$50.4\pm 4.7$	39.4
[O III]	4363	$1.4\pm 0.4$	1.5
He I	4471	$8.8\pm 0.4$	8.1
[O III]	4959	$81.3\pm 1.7$	82.1
[O III]	5007	$242.9\pm 4.9$	245.1
[Cl III]	5518	$0.5\pm 0.1$	0.6
[Cl III]	5538	$0.4\pm 0.1$	0.4
[N II]	5755	$1.3\pm 0.1$	2.2
He I	5876	$25.8\pm 0.7$	23.6
[N II]	6548	$41.8\pm 1.2$	51.0
H $\alpha$	6563	$301.6\pm 9.0$	286.8
[N II]	6583	$130.3\pm 3.9$	150.3
He I	6678	$7.0\pm 0.4$	5.9
[S II]	6716	$5.1\pm 0.3$	4.4
[S II]	6731	$4.2\pm 0.3$	3.6
He I	7065	$4.2\pm 0.5$	4.2
[Ar III]	7136	$15.2\pm 0.7$	26.1
$c(H\beta)$		$0.62\pm 0.03$	0.65
$\log(F(H\beta))$	[erg s <sup>-1</sup> cm <sup>-2</sup> ]	$-13.01\pm 0.01$	-13.01
$n_e$ ([S II])	[cm <sup>-3</sup> ]	$200\pm 140$	198
$T_e$ ([O III])	[K]	$9550\pm 820$	9708

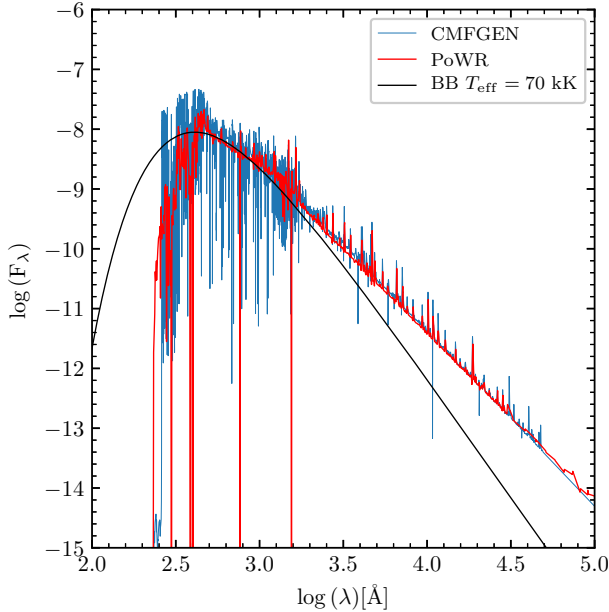
observations. Their slit A6 is placed on a region spatially coincident with the one used here to estimate the total IR photometry of NGC 6888 (see Figure 1 in [Esteban, et al. 2016](#)). Their abundances and emission line fluxes obtained from these observations are listed in Tables 4 and 5, respectively. The total  $H\beta$  flux ( $F(H\beta)$ ) in logarithmic scale, the electron temperature ( $T_e$ ) and  $n_e$  obtained from the [O III] and [S II] lines, respectively, are also presented in the bottom rows of Table 5. We note that during the fitting process, some of the abundances had to be tuned in order to reproduce simultaneously the optical and IR emission lines. For comparison we also show in Table 4 the abundances reported by other works.

We demonstrated in Paper I that a detailed prescription of the stellar atmosphere is necessary to obtain a more realistic description of the nebular and dust parameters. The progenitor star of NGC 6888, WR 136, has been modeled by [Hamann, et al. \(2019\)](#) using the updated version of the stellar atmosphere code PoWR. The best fit stellar parameters reported in that work are listed in Table 6. Accord-



**Table 6.** Principal stellar parameters of WR 136.

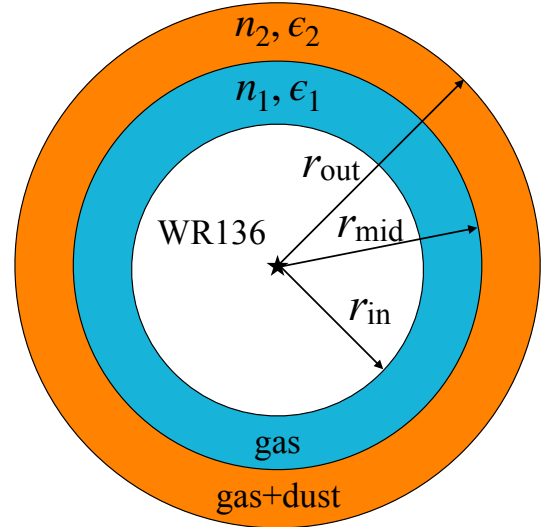
$d$ [kpc]	$1.9^{+0.14}_{-0.12}$	Bailer-Jones et al. (2018)
WR-subtype	WN6h	Hamann, et al. (2019)
$M_*$ [ $M_\odot$ ]	23/21	Hamann, et al. (2019)
$\log(L)$ [ $L_\odot$ ]	5.78	Hamann, et al. (2019)
$T_*$ [kK]	70.8	Hamann, et al. (2019)


**Figure 7.** Comparison between different stellar atmosphere models. The blue line correspond to the stellar atmosphere from CMFGEN used in Reyes-Pérez et al. (2015) while the red line is the PoWR model used in the present work. The black line presents a blackbody emission model with an effective temperature of 70 kK.

ingly, we retrieved the model labelled as WNL 10-16 with Galactic metallicity and hydrogen fraction of 0.2 from the PoWR database. This model is presented in Figure 7 compared to a blackbody emission model with the same effective temperature (70 kK) as well as the stellar model used by Reyes-Pérez et al. (2015) kindly provided by J. Reyes-Pérez. In the following, we will adopt the distance of  $d = 1.9^{+0.14}_{-0.12}$  kpc estimated by Bailer-Jones et al. (2018) using the *Gaia* data release.

### 6.1 Detailed modeling of NGC 6888

The  $H\alpha$  and [N II] images of NGC 6888 show an apparent elliptical shape with semi-major and semi-minor axes of  $540''$  and  $360''$ , respectively. At a distance of 1.9 kpc, the physical size of NGC 6888 is 5 pc and 3.9 pc, respectively. Marston & Meaburn (1988) showed however that the kinematics of NGC 6888 can be broadly fit by an expanding spherical shell with an expansion velocity of  $85 \text{ km s}^{-1}$ , although we note that a shell with blisters would be more accurate as unveiled by the [O III] image. For this, we adopted a spherically-symmetric shell for our model. An averaged angular radius of  $450''$  was set as a fixed parameter for the outer radius ( $r_{\text{out}}$ ). The inner radius ( $r_{\text{in}}$ ) was varied along with the filling factor ( $\epsilon$ ) and  $n_e$  to try


**Figure 8.** Schematic view of the two-shell density distribution used to model the nebular and IR properties of NGC 6888. The outer shell accounts for the presence of gas and dust while the inner shell only contains gas.

to fit the optical observations and physical properties of NGC 6888. Values between  $n_e \lesssim 100 - 500 \text{ cm}^{-3}$  for the electron density have been reported in the literature (Esteban & Vilchez 1992; Fernández-Martín et al. 2012; Esteban, et al. 2016, see also Table 3), but we note that it is very likely that the largest values correspond to dense clumps detected in  $H\alpha$  and [N II] narrow-band images (see Fig. 1).

We performed a large number of models fixing  $r_{\text{out}}$  but varying  $r_{\text{in}}$  for families of  $n_e$  values. None of these models resulted in good nebular parameters comparable to those reported for NGC 6888. Consequently, we followed the results from Reyes-Pérez et al. (2015) and considered two shells: an inner shell with density  $n_1$  between  $r_{\text{in}}$  and  $r_{\text{mid}}$  and a filling factor  $\epsilon_1$  composed purely of gas, and an outer shell with density  $n_2$  between  $r_{\text{mid}}$  and  $r_{\text{out}}$  and  $\epsilon_2$ . The outer shell includes contributions from both gas and dust. A schematic view of this model is presented in Figure 8.

Our best model that reproduces the nebular properties of NGC 6888 was achieved with  $n_1 = 400 \text{ cm}^{-3}$ ,  $n_2 = 180 \text{ cm}^{-3}$ ,  $\epsilon_1 = 10^{-3}$ ,  $\epsilon_2 = 0.07$ . The radii are  $r_{\text{in}} = 400''$ ,  $r_{\text{mid}} = 425''$ , and  $r_{\text{out}} = 450''$ . The synthetic intensities of the most important optical lines are listed in Table 5 in comparison with those reported in Esteban, et al. (2016) for their slit A6. The emission IR lines obtained from our model are compared to those obtained from the *Spitzer* IRS observations in Table 3. Despite the variations obtained from the *Spitzer* IRS spectra, the model broadly reproduces the IR lines, corroborating previous findings that suggest that the inner regions of NGC 6888 are dominated by photoionization (Esteban & Vilchez 1992; Esteban et al. 1993; Reyes-Pérez et al. 2015). Although we note that there might be certain components associated to shocks which produce line excitation (Moore, Hester & Scowen 2000; Gruendl et al. 2000).

As noted before, we started our fitting process by adopting the set of abundances reported for slit A6 by Esteban, et al. (2016). However, some elemental abundances required small changes in order to fit both the optical and IR emission lines. Nevertheless, most of them resulted in values close to those reported in the literature. In particular, the O abundance had to be reduced to 8.05, a small value

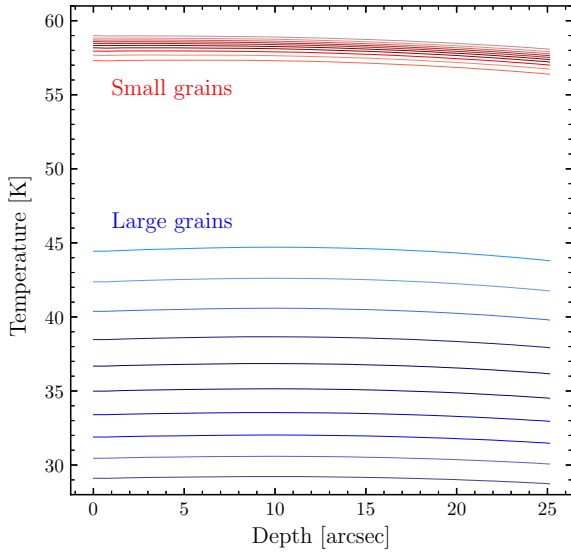


**Figure 9.** Temperature distribution for the different dust sizes used for our best model of NGC 6888. Each line represents a size bin of the small ( $a_{\text{small}}=[0.002\text{--}0.008]\ \mu\text{m}$ ) and large grains ( $a_{\text{big}}=[0.05\text{--}0.5]\ \mu\text{m}$ ).

compared to what has been reported by the references in Table 4, but marginally similar to the lower value reported by Esteban, et al. (2016). The last column in Table 4 lists the final abundances used for our best model.

Once we have modeled the observed emission lines of NGC 6888 we now include dust in our calculations to produce synthetic IR photometry. During the RSG and LBV phase, massive stars are copious producers of oxygen which condensate molecules, such as silicates in their atmospheres (Dharmawardena et al. 2020; Verhoelst et al. 2009). Accordingly, we adopt grains composed of amorphous astronomical silicate. In particular, Cloudy includes olivine ( $\text{MgFeSiO}_4$ ) as the default silicate grain.

Initially, we used two distribution of dust sizes as those used in Mathis, Casinelli & van der Hucht (1992): a distribution for small grains with sizes  $a_{\text{small}}=[0.002\text{--}0.008]\ \mu\text{m}$  and another for big grains with sizes  $a_{\text{big}}=[0.005\text{--}0.25]\ \mu\text{m}$ . However, our first attempts to model the IR SED suggested the need of extending the size of the large grains. Finally, we found that a population of sizes for the big grains of  $a_{\text{big}}=[0.05\text{--}0.50]\ \mu\text{m}$  improved our model. The maximum size of the big grains was fixed to  $0.50\ \mu\text{m}$  as found for the RSG star VY Canis Majoris (Sciocluna et al. 2015). In all cases, the grains are spherical and their sizes follow a Mathis et al. (1977) power-law distribution  $\propto a^{-3.5}$  with 10 size bins for each distribution.

To reproduce the observed IR SED, our model requires a large amount of big grains, with a big grains-to-small grains ratio of 16:1 and a resultant dust-to-gas ratio of  $5.6 \times 10^{-3}$ . The synthetic photometry obtained from our model is compared to the observed IR SED in Figure 6. Our best model suggests that the total mass of NGC 6888 is  $25.5^{+4.7}_{-2.8} M_{\odot}$  with a total dust mass of  $M_{\text{dust}} = 0.14^{+0.03}_{-0.01} M_{\odot}$ , less than a half of that estimated by the MBB model with fixed  $\beta = 2$ . The model predicts a mass for the big grains of  $0.134^{+0.03}_{+0.01} M_{\odot}$ . We note that the errors in the total mass and dust mass estimates were

obtained by propagating the errors in the distance as reported by Bailer-Jones et al. (2018).

In Figure 9 we show the temperature distribution for different bin sizes of the dust grains located in the outer shell. The temperature for the large grains is in the range estimated using the MBB approximation.

## 7 DISCUSSION

### 7.1 On the spatial distribution of dust in NGC 6888

Our analysis above has disclosed an unprecedented view of the IR emission of the WR nebula NGC 6888. The *Herschel* PACS and *Spitzer* IRAC images have revealed in great detail the distribution of dust in this WR nebula and the ISM around it. These are shown in the colour-composite IR panels of Figure 1 which are compared to the optical image of NGC 6888. Such detailed morphological IR characteristics of NGC 6888 are only allowed by the spatial resolution of the observations used here as compared with the *IRAS* images used in previous analyses (Marston 1991; Mathis, Casinelli & van der Hucht 1992).

An interesting feature seen in the IR panels in Figure 1 is a gap between the dust in NGC 6888 and the emission that traces the outer cold dust from the ISM. This situation is clearly seen in the NE cap of NGC 6888 and to a lesser extent towards the SW cap. For example, Figure 1 bottom right panel shows a dark region separating the *Herschel* images at  $70\ \mu\text{m}$  and  $160\ \mu\text{m}$ . A careful comparison between the [O III] and IR images of the nebula shows that the former is distributed exactly in the dark region observed in the colour-composite IR panels of this figure (see Appendix A).

Gruendl et al. (2000) presented the analysis of  $\text{H}\alpha$  and [O III] narrow-band images of a sample of 8 bright WR nebulae, including NGC 6888. They showed that the [O III] emission is smooth and traces the leading shock of the expanding nebula, while the  $\text{H}\alpha$  emission displays a clumpy morphology trailing inside the [O III] emission (see Fig. 1 top left panel). Gruendl et al. (2000) argued that the displacement between these two emission lines is due to radiative cooling. Behind the shock front, the temperature drops while the density increases displacing the two emissions. We suggest that this dark region, which is coincident with the [O III] leading shock, is unveiling the destruction of dust at the edge of NGC 6888.

The destruction of dust grains may be due to thermal evaporation, gas-grain collisions and destruction by grain-grain collisions (see Woitke, Dominik & Sedlmayr 1993). According to Jones, et al. (1996) the destruction of silicate dust grains in low velocity shocks can be attributed to non-thermal sputtering while large grains ( $\sim 0.1\ \mu\text{m}$ ) are easily shattered in grain-grain collisions. Slavin et al. (2004) presented calculations on the dust-gas decoupling on dust destruction in shocks. They found that grains with a large range of sizes are almost completely destroyed by shock waves with velocities around  $75\text{--}150\ \text{km s}^{-1}$ . The reported expansion velocity of NGC 6888,  $\sim 80\ \text{km s}^{-1}$  (Chu et al. 1983; Marston & Meaburn 1988), makes plausible the destruction of dust at the edge of NGC 6888 as the nebula expands.

### 7.2 Consequences of the dust model

Taking advantage of an improved analysis of the spatial distribution of dust in NGC 6888, we managed to uncover its true IR SED. This represents an improvement over the nebular estimates made from



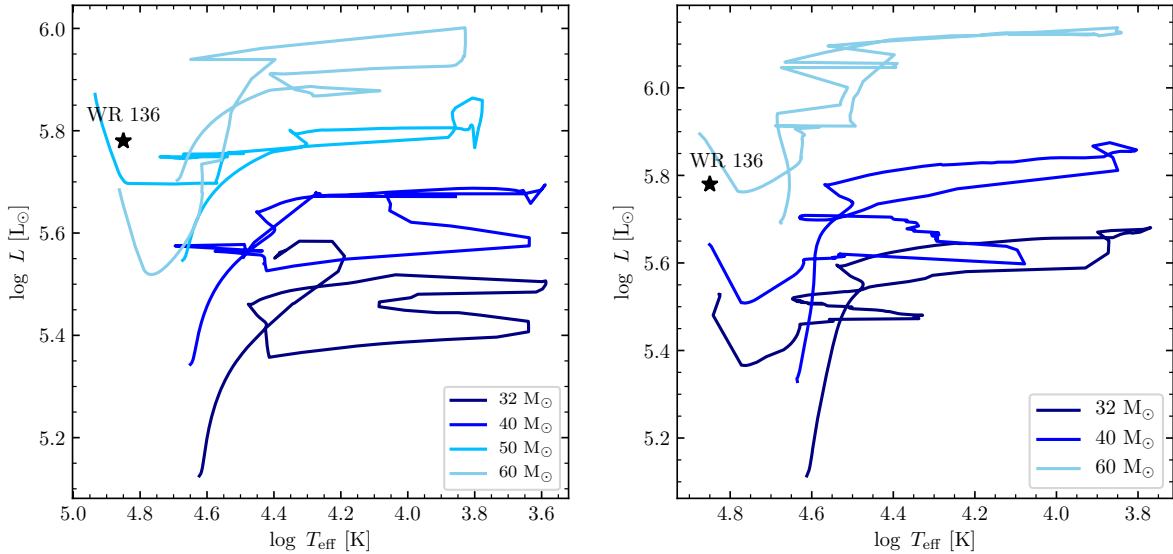


**Figure 10.** Hertzsprung–Russell diagrams of stellar evolution models with initial masses between 30 and 60  $M_{\odot}$  from Ekström et al. (2012). The black star represents the position of WR 136. Different colours represent models from different initial masses. The left (right) panel presents model without (with) stellar rotation. There is no star model available with initial mass of 50  $M_{\odot}$  in the Geneva Code web page.

low-resolution *IRAS* observations. Our best model is able to reproduce nebular optical and IR properties of NGC 6888 using an appropriate description of the stellar atmosphere of WR 136. This resulted in a total mass of NGC 6888 of  $25.5^{+4.7}_{-2.8} M_{\odot}$  with a dust-to-gas ratio of  $5.6 \times 10^{-3}$ , that is, a total dust mass of  $M_{\text{dust}} = 0.14^{+0.03}_{-0.01} M_{\odot}$ . If we assume a duration of  $2 \times 10^5$  yr for the RSG phase, we can estimate an averaged mass-loss rate of  $(1.28^{+0.23}_{-0.15}) \times 10^{-4} M_{\odot} \text{ yr}^{-1}$ , consistent with that expected for the RSG phase.

Our results represent an improvement to the work of Mathis, Casinelli & van der Hucht (1992). They tried to fit simultaneously the nebular properties and the low-spatial resolution *IRAS* observations of NGC 6888. We have shown that their SED overestimated the real IR flux from this WR nebula. Although the estimated mass is of the same order as that estimated by our model (20  $M_{\odot}$ ), they used a blackbody model for the stellar radiation field with  $T_{\text{eff}} = 50$  kK. These authors restricted the large size of their big grains to  $0.25 \mu\text{m}$  but we found that increasing it to  $0.5 \mu\text{m}$  improved significantly our comparison with the IR SED. The limit of  $0.5 \mu\text{m}$  was set following the findings of Scicluna et al. (2015) on the RSG VY Canis Majoris. We note that a smaller population of big grains did not result in a good fit to the IR SED. In addition we tried models with dust sizes larger than  $0.5 \mu\text{m}$  without significant improvement. It is important to note that 93% of the dust mass corresponds to grains with sizes similar as those obtained for RSG stars (larger than those estimated for the ISM). That is, we are detecting the material ejected in the previous RSG phase with negligible contribution from swept up ISM material.

It seems indeed that the total mass of the nebula corresponds to material ejected by WR 136 in its previous RSG phase without any contribution from swept-up ISM material as suggested by the analysis of the IR images. Adopting a current mass for WR 136 of  $\sim 22 M_{\odot}$  (see Table 5; Hamann, et al. 2019) one can estimate its initial mass to be  $\lesssim 50 M_{\odot}$ . This is corroborated by the stellar evolutionary mod-

els presented by Ekström et al. (2012)<sup>5</sup>. In Figure 10 we present HR diagrams obtained by using stellar evolution models at  $Z = 0.014$  with and without rotation with initial masses between 32 and 60  $M_{\odot}$ . The stellar parameters ( $T_{\text{eff}}$  and  $L$ ) estimated from the PoWR stellar atmosphere models (Hamann, et al. 2019) are somewhat consistent with WR 136 having an initial mass of 50  $M_{\odot}$ . Abundance estimates, in particular the He versus C/O diagram presented by Esteban, et al. (2016), are also consistent with this finding (see Figure 9 in that paper). Finally, we calculated the averaged mass-loss rate predicted for a 50  $M_{\odot}$  stellar evolution model. This resulted in  $1.9 \times 10^{-4} M_{\odot}$ , very similar to that estimated using our detailed model.

We note that other authors have estimated ionized masses of  $\sim 4 M_{\odot}$  (see Marston & Meaburn 1988; Kwitter 1981; Wendker et al. 1975) for NGC 6888 using radio and  $H\alpha$  line emission. We have recalculated their estimates by following the procedure in Marston & Meaburn (1988) using the  $H\alpha$  intensity with the current distance of 1.9 kpc and an electron density of  $180 \text{ cm}^{-3}$  as obtained for the dominant shell in our model (also consistent with observations). This resulted in  $21.9^{+7.2}_{-5.0} M_{\odot}$ , which is consistent with the total estimated mass from our Cloudy model, but slightly smaller. This seems to suggest that NGC 6888 is almost completely ionized. If the difference,  $3.6 M_{\odot}$ , is considered to be neutral material, this should be shielded from the UV radiation from WR 136 in the dense clumps and filaments seen in the  $H\alpha + [\text{N II}]$  images.

It is not necessary to invoke a contribution from the ISM in the mass of NGC 6888. An appropriate distance estimation by means of the *Gaia* observations, and improvement of the stellar evolution models, and a careful dissection of the IR SED have allowed us to conclude that the origin of this WR nebula is purely due to processed ejected stellar wind.

We would like to point out that in order to produce a consistent model of WR nebulae one must take into account important aspects

<sup>5</sup> The models were retrieved from the Geneva Code webpage: <https://www.unige.ch/sciences/astro/evolution/en/database/>.

such as an appropriate description of the WR stellar atmosphere of the progenitor star and the simultaneous treatment of gas and dust (see Paper I). In particular we note here that the density distribution of our model was initially based on the findings reported by Reyes-Pérez et al. (2015) which only modeled the photoionized structure of NGC 6888.

Although these authors used a very similar WR stellar atmosphere as that used in the present work (see Fig. 7), the inclusion of dust in the model requires some tuning to the density parameters to simultaneously fit the optical and IR observations.

Finally, we note that our model predictions have been compared to single stellar evolution models, but it is currently accepted that massive stars are born in binary systems affecting their evolution (see Section 1). However, there is no observational evidence that WR 136 is a binary star (see Fullard et al. 2020; Gräfener et al. 2012) and the clumpy morphology of its associated WR nebula seems to have been the result of instabilities produced by the wind-wind interaction scenario, in contrast to the ballistic expanding clumps expected in a common envelope stripping scenario (see discussion in Paper I).

## 8 CONCLUSIONS

We presented a characterization of the distribution and properties of dust in the WR nebula NGC 6888 around WR 136. We used archival IR observations (spectra and images) that cover the 3–160  $\mu\text{m}$  wavelength range in conjunction with the photoionization code *CLOUDY* to model simultaneously the properties of the ionized and dust components in NGC 6888. Our findings can be summarized as:

- The combination of the IR images allowed us to perform an unprecedented study of the spatial distribution of dust in NGC 6888. The high-resolution IR images used here helped us to dissect the contribution from dust in NGC 6888 and that corresponding to the ISM. We discovered a dark region between the IR emission at the outer edge of the WR nebula coincident with the [O III] optical emission. We suggest that this dark region is unveiling the destruction of dust at the edge of NGC 6888 due to its relatively high expansion velocity ( $\sim 80 \text{ km s}^{-1}$ ).

- The IR photometry extracted taking into account the nebular morphology of NGC 6888 is heavily contaminated by the contribution from ISM clouds and filaments, a problem that could not be properly resolved in previous IR studies of this WR nebula. By studying the IR SED from different regions within NGC 6888 and its immediate surroundings, we suggest that the NW region has no contamination from the ISM. The true IR SED of NGC 6888 peaks between 70  $\mu\text{m}$  and 100  $\mu\text{m}$ , very similar to other WR nebulae.

- Our best model to the nebular parameters and IR SED was achieved by adopting a spherical two-shell distribution with inner and outer densities of  $n_1 = 400 \text{ cm}^{-3}$  and  $n_2 = 180 \text{ cm}^{-3}$  and filling factors of  $10^{-3}$  and 0.07, respectively. We adopted two population of dust grains with sizes  $a_{\text{small}} = [0.002\text{--}0.008] \mu\text{m}$  and  $a_{\text{big}} = [0.05\text{--}0.50] \mu\text{m}$ , the later in line with the large dust grains in the RSG star VY Canis Majoris. The total dust mass in NGC 6888 resulted in  $0.14^{+0.03}_{-0.01} M_{\odot}$  with a dust-to-gas ratio of  $5.6 \times 10^{-3}$ . The small grains contribute to 6% of the total dust mass.

- We found that the dust in NGC 6888 is dominated by large dust with RSG origin which suggest that this WR nebula is mainly composed by material ejected by the star with negligible contribution from swept up ISM.

- The total estimated mass of NGC 6888 is  $25.5^{+4.7}_{-2.8} M_{\odot}$ , together with the estimates from Hamann, et al. (2019) for its progenitor star, leads us to suggest an initial mass  $\lesssim 50 M_{\odot}$  for WR 136. This result

is supported by stellar evolution models, in particular the prediction of the mass-loss rate and the abundance determinations reported in the literature.

## ACKNOWLEDGMENTS

The authors would like to thank the referee, Anthony P. Marston, for comments and suggestions that improved the presentation of this paper. The authors are also thankful to J. Reyes-Pérez for providing the *CMFGEN* model of WR 136. G.R. would like to thank S.J. Arthur and people at IRyA-UNAM for their support during the realization of this project. G.R., E.S and J.A.Q.-M. acknowledge support from Consejo Nacional de Ciencia y Tecnología (CONACyT) for student scholarship. J.A.T., G.R., and M.A.G. are funded by UNAM DGAPA PAPIIT project IA100720. M.A.G. acknowledges support of the Spanish Ministerio de Ciencia, Innovación y Universidades grant PGC2018-102184-B-I00, co-funded by FEDER funds. G.R.-L. acknowledges support from CONACyT and PRODEP (Mexico). VMAGG acknowledges support from the Programa de Becas posdoctorales of DGAPA UNAM. This work makes use of *IRAF*, distributed by the National Optical Astronomy Observatory, which is operated by the Association of Universities for Research in Astronomy under cooperative agreement with the National Science Foundation. This work makes use of *Herschel*, *Spitzer* and *WISE* IR observations. *Herschel* is an ESA space observatory with science instruments provided by European-led Principal Investigator consortia and with important participation from NASA. The *Spitzer* Space Telescope was operated by the Jet Propulsion Laboratory, California Institute of Technology under a contract with NASA. Support for this work was provided by NASA through an award issued by JPL/Caltech. *WISE* is a joint project of the University of California (Los Angeles, USA) and the JPL/Caltech, funded by NASA.

## DATA AVAILABILITY

The data underlying this article will be shared on reasonable request to the corresponding author.

## REFERENCES

- Arnal, E. M. & Cappa, C. E. 1996, *MNRAS*, 279, 788  
 Bailer-Jones, C. A. L., Rybizki, J., Fouesneau, M., et al. 2018, *AJ*, 156, 58  
 Cappa, C. E., Dubner, G. M., Rogers, C., et al. 1996, *AJ*, 112, 1104  
 Cichowski, S., Duronea, N. U., Suad, L. A., et al. 2020, *MNRAS*, 495, 417  
 Chu, Y.-H., Treffers, R. R., & Kwitter, K. B. 1983, *ApJS*, 53, 937  
 Chu, Y.-H. 1981, *ApJ*, 249, 195  
 Cox, N. L. J., Kerschbaum, F., van Marle, A.-J., et al. 2012, *A&A*, 537, A35  
 Dharmawardena, T. E., Mairs, S., Scicluna, P., et al. 2020, *ApJ*, 897, L9  
 Draine B. T., 2003, *ARA&A*, 41, 241  
 Ekström, S., Georgy, C., Eggenberger, P., et al. 2012, *A&A*, 537, A146  
 Eldridge, J. J., Stanway, E. R., Xiao, L., et al. 2017, *Publ. Astron. Soc. Australia*, 34, e058  
 Esteban C., Mesa-Delgado A., Morisset C., García-Rojas J., 2016, *MNRAS*, 460, 4038  
 Esteban, C., Smith, L. J., Vilchez, J. M., et al. 1993, *A&A*, 272, 299  
 Esteban, C., & Vilchez, J. M. 1992, *ApJ*, 390, 536  
 Fang, X., Zhang, Y., Kwok, S., et al. 2018, *ApJ*, 859, 92  
 Fang, X., Guerrero, M. A., Toalá, J. A., et al. 2016, *ApJ*, 822, L19  
 Ferland, G. J., Chatzikos, M., Guzmán, F., et al. 2017, *Rev. Mex. Astron. Astrofis.*, 53, 385  
 Fernández-Martín A., Martín-Gordón D., Vilchez J. M., Pérez Montero E., Riera A., Sánchez S. F., 2012, *A&A*, 541, A119

Fullard, A. G., St-Louis, N., Moffat, A. F. J., et al. 2020, *AJ*, 159, 214  
 Freyer, T., Hensler, G., & Yorke, H. W. 2006, *ApJ*, 638, 262  
 García-Segura, G., & Mac Low, M.-M. 1995, *ApJ*, 455, 145  
 García-Segura, G., Langer, N., & Mac Low, M.-M. 1996, *A&A*, 316, 133  
 Götzberg, Y., de Mink, S. E., Groh, J. H., et al. 2018, *A&A*, 615, A78  
 Gräfener, G., Vink, J. S., Harries, T. J., et al. 2012, *A&A*, 547, A83  
 Groenewegen, M. A. T., Waelkens, C., Barlow, M. J., et al. 2011, *A&A*, 526, A162  
 Gruendl, R. A., Chu, Y.-H., & Guerrero, M. A. 2004, *ApJ*, 617, L127  
 Gruendl, R. A., Chu, Y.-H., Dunne, B. C., & Points, S. D. 2000, *AJ*, 120, 2670  
 Gvaramadze, V. V., Kniazev, A. Y., & Fabrika, S. 2010, *MNRAS*, 405, 1047  
 Hamann W.-R., et al., 2019, *A&A*, 625, A57  
 Hamann, W.-R., Gräfener, G., & Liermann, A. 2006, *A&A*, 457, 1015  
 Hamann, W.-R., & Gräfener, G. 2004, *A&A*, 427, 697  
 Hillier, D. J., & Miller, D. L. 1998, *ApJ*, 496, 407  
 Houck J. R., et al., 2004, *SPIE*, 62, SPIE .5487  
 Ivanova, N. 2011, *ApJ*, 730, 76  
 Jiménez-Hernández, P., Arthur, S. J., & Toalá, J. A. 2020, Accepted to *MNRAS*, arXiv:2007.14373, Paper I  
 Jones A. P., Tielens A. G. G. M., Hollenbach D. J., 1996, *ApJ*, 469, 740  
 Juvela, M., Montillaud, J., Ysard, N., et al. 2013, *A&A*, 556, A63  
 Kochanek, C. S. 2011, *ApJ*, 743, 73  
 Kwitter, K. B. 1981, *ApJ*, 245, 154  
 Lü, G., Zhu, C., & Podsiadlowski, P. 2013, *ApJ*, 768, 193  
 Luridiana, V., Morisset, C., & Shaw, R. A. 2015, *A&A*, 573, A42  
 Marchenko, S. V., Moffat, A. F. J., Vacca, W. D., et al. 2002, *ApJ*, 565, L59  
 Marston, A. P., Welzmler, J., Bransford, M. A., et al. 1999, *ApJ*, 518, 769  
 Marston, A. P. 1996, *AJ*, 112, 2828  
 Marston, A. P. 1995a, *AJ*, 109, 1839  
 Marston, A. P. 1995b, *AJ*, 109, 2257  
 Marston A. P., 1991, *ApJ*, 366, 181  
 Marston, A. P., & Meaburn, J. 1988, *MNRAS*, 235, 391  
 Mason, B. D., Hartkopf, W. I., Gies, D. R., et al. 2009, *AJ*, 137, 3358  
 Mathis, J. S., Rimpl, W., & Nordsieck, K. H. 1977, *ApJ*, 217, 425  
 Mathis J. S., Cassinelli J. P., van der Hucht K. A., Prusti T., Wesselius P. R., Williams P. M., 1992, *ApJ*, 384, 197  
 Méndez-Delgado, J. E., Esteban, C., García-Rojas, J., et al. 2020, *MNRAS*, 496, 2726  
 Mesa-Delgado A., Esteban C., García-Rojas J., Reyes-Pérez J., Morisset C., Bresolin F., 2014, *ApJ*, 785, 100  
 Moore B. D., Hester J. J., Scowen P. A., 2000, *AJ*, 119, 2991  
 Morisset, C. 2013, *pyCloudy: Tools to manage astronomical Cloudy photoionization code*, ascl:1304.020  
 Morris, P. W., Gull, T. R., Hillier, D. J., et al. 2017, *ApJ*, 842, 79  
 Mata, H., Ramos-Larios, G., Guerrero, M. A., et al. 2016, *MNRAS*, 459, 841  
 Ostrovskii A. B., Parfenov S. Y., Vasyunin A. I., Ivlev A. V., Sokolova V. A., 2020, *MNRAS*, 495, 4314  
 Reyes-Pérez J., Morisset C., Peña M., Mesa-Delgado A., 2015, *MNRAS*, 452, 1764  
 Sana, H., de Mink, S. E., de Koter, A., et al. 2012, *Science*, 337, 444  
 Scicluna, P., Siebenmorgen, R., Wesson, R., et al. 2015, *A&A*, 584, L10  
 Slavin, J. D., Jones, A. P., & Tielens, A. G. G. M. 2004, *ApJ*, 614, 796  
 Smith, J.D.T., Armus, L., Dale, A., et al. 2007, *PASP*, 119, 1133  
 Smith J. D. T., et al., 2007, *ApJ*, 656, 770  
 St-Louis, N., Doyon, R., Chagnon, F., et al. 1998, *AJ*, 115, 2475  
 Stock, D. J., & Barlow, M. J. 2014, *MNRAS*, 441, 3065  
 Stock, D. J., & Barlow, M. J. 2010, *MNRAS*, 409, 1429  
 Toalá, J. A., Ramos-Larios, G., Guerrero, M. A., et al. 2019, *MNRAS*, 485, 3360  
 Toalá, J. A., Marston, A. P., Guerrero, M. A., et al. 2017, *ApJ*, 846, 76  
 Toalá, J. A., Guerrero, M. A., Chu, Y.-H., et al. 2016, *MNRAS*, 456, 4305  
 Toalá, J. A., Guerrero, M. A., Ramos-Larios, G., et al. 2015, *A&A*, 578, A66  
 Toalá, J. A., Guerrero, M. A., Gruendl, R. A., et al. 2014, *AJ*, 147, 30  
 Toalá, J. A., Guerrero, M. A., Chu, Y.-H., et al. 2012, *ApJ*, 755, 77  
 Toalá, J. A., & Arthur, S. J. 2011, *ApJ*, 737, 100  
 Tody, D. 1993, *Astronomical Data Analysis Software and Systems II*, 173  
 Tuthill, P. G., Monnier, J. D., & Danchi, W. C. 1999, *Nature*, 398, 487

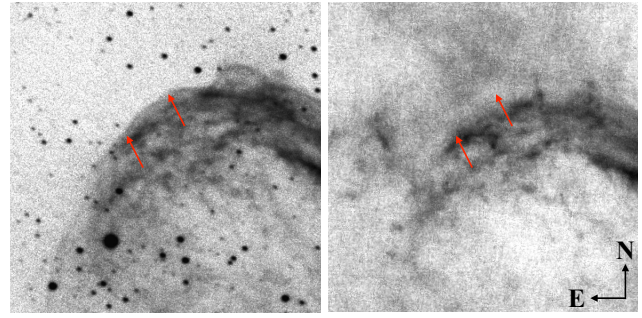


**Figure A1.** Close-up of the NE cap of NGC 6888. Grey scale images of the optical [O III] narrow-band filter (left) and the *Herschel* PACS 70  $\mu\text{m}$  (right) showing the gap (lack of emission) described in Section 3. The red arrows show the edge of the [O III] in both panels. Both panels have the same FoV.

van Buren, D., & McCray, R. 1988, *ApJ*, 329, L93  
 van der Hucht, K. A. 2001, *New Astron. Rev.*, 45, 135  
 Vamvatira-Nakou, C., Hutsemékers, D., Royer, P., et al. 2016, *A&A*, 588, A92  
 Verhoelst, T., van der Zypen, N., Hony, S., et al. 2009, *A&A*, 498, 127  
 Wachter, S., Mauerhan, J. C., Van Dyk, S. D., et al. 2010, *AJ*, 139, 2330  
 Weis, K. 2001, *Reviews in Modern Astronomy*, 14, 261  
 Wendker, H. J., Smith, L. F., Israel, F. P., et al. 1975, *A&A*, 42, 173  
 Woitke P., Dominik C., Sedlmayr E., 1993, *A&A*, 274, 451  
 Wrigge, M., Chu, Y.-H., Magnier, E. A., et al. 2005, *ApJ*, 633, 248

## APPENDIX A: DUST DESTRUCTION AT THE EDGE OF NGC 6888

To further illustrate the correlation between the gap region surrounding NGC 6888 detected in IR images and that of the nebular emission, we have created close-up, grey-scale images of the optical [O III] and that of the *Herschel* PACS 70  $\mu\text{m}$  of the NE region. The images presented in Figure A1, show with red arrows the position of the [O III] emission.